Aerospace Science and Technology 45 (2015) 17–29

Contents lists available at ScienceDirect

Aerospace Science and Technology

www.elsevier.com/locate/aescte

Multi-fidelity robust aerodynamic design optimization under mixed uncertainty

Harsheel Shah [a,*,1], Serhat Hosder [a,2], Slawomir Koziel [b,3], Yonatan A. Tesfahunegn [c,4], Leifur Leifsson [d,5]

[a] Missouri University of Science & Technology, Rolla, MO 65409, USA
[b] Gdansk University of Technology, 80-233 Gdansk, Poland
[c] Reykjavik University, Menntavegur 1, 101 Reykjavik, Iceland
[d] Iowa State University, Ames, IA 50011, USA

ARTICLE INFO

Article history:
Received 6 February 2015
Received in revised form 15 April 2015
Accepted 19 April 2015
Available online 22 April 2015

Keywords:
Multi-fidelity modeling
Polynomial chaos
Computational fluid dynamics
Aerodynamic shape optimization
Robust design
Output space mapping

ABSTRACT

The objective of this paper is to present a robust optimization algorithm for computationally efficient airfoil design under mixed (inherent and epistemic) uncertainty using a multi-fidelity approach. This algorithm exploits stochastic expansions derived from the Non-Intrusive Polynomial Chaos (NIPC) technique to create surrogate models utilized in the optimization process. A combined NIPC expansion approach is used, where both the design and the mixed uncertain parameters are the independent variables of the surrogate model. To reduce the computational cost, the high-fidelity Computational Fluid Dynamics (CFD) model is replaced by a suitably corrected low-fidelity one, the latter being evaluated using the same CFD solver but with a coarser mesh. The model correction is implemented to the low-fidelity CFD solutions utilized for the construction of stochastic surrogate by using multi-point Output Space Mapping (OSM) technique. The proposed algorithm is applied to the design of NACA 4-digit airfoils with four deterministic design variables (the airfoil shape parameters and the angle of attack), one aleatory uncertain variable (the Mach number) and one epistemic variable (β, a geometry parameter) to demonstrate robust optimization under mixed uncertainties. In terms of computational cost, the proposed technique outperforms the conventional approach that exclusively uses the high-fidelity model to create the surrogates. The design cost reduces to only 34 equivalent high-fidelity model evaluations versus 168 obtained with the conventional method.

1. Introduction

Robust Design is a design methodology for improving the quality of a product by minimizing the impact of uncertainties on the product performance. The objective of robust design is to optimize the mean performance while minimizing the variation of performance caused by various uncertainties. In the context of aerodynamic shape optimization, robust design implies that the performance (such as coefficient of drag, the lift-to-drag ratio, etc.) of the final configuration should be insensitive to the uncertainties in the operating conditions (e.g., free-stream Mach number) and the geometry (e.g., manufacturing uncertainties). An important component of robust design is Uncertainty Quantification (UQ), which may significantly increase the computational expense of the design process compared to the computational effort of deterministic optimization. This is particularly the case when high-fidelity analysis tools are involved in the design process in order to ensure sufficient accuracy. Therefore, it is important to develop and implement computationally efficient robust design methodologies while keeping the desired accuracy level in the optimization process.

Two types of input uncertainty should be considered in robust aerodynamic design studies: inherent (aleatory) uncertainty and epistemic uncertainty [1,2]. Aleatory uncertainty, which is probabilistic and irreducible, describes the inherent variation associated with the physical system (e.g., the operating conditions). Epistemic uncertainty [3] is reducible and described as lack of knowledge or information in any phase or operation of a design process (e.g., turbulence models used in CFD simulations). These two types of uncertainties usually co-exist (e.g., mixed uncertainties) in real-world

* Corresponding author.
E-mail address: hrsvff@mst.edu (H. Shah).
[1] Ph.D. Candidate, Department of Mechanical and Aerospace Engineering.
[2] Associate Professor, Department of Mechanical and Aerospace Engineering.
[3] Visiting Professor of Science.
[4] Post-Doctoral Research Fellow.
[5] Assistant Professor, Department of Aerospace Engineering.

http://dx.doi.org/10.1016/j.ast.2015.04.011
1270-9638/

Nomenclature

n	number of design variables
N	number of random variables
p_d	deterministic state variable vector
SR	support region of random input variable
n_p	oversampling ratio
p	order of polynomial chaos
$\boldsymbol{\xi}$	standard input random variable vector
$p(\boldsymbol{\xi})$	probability density function of $\vec{\xi}$
ψ	random basis function
a	coefficient in polynomial chaos expansion
a^*	stochastic function
μ	mean
σ	standard deviation
N_t	number of terms in a total-order expansion
C_l	coefficient of lift
C_d	coefficient of drag
M	Mach number
α	angle of attack in degrees
β	geometry parameter in thickness distribution formula for NACA 4-digit airfoils
Re	Reynolds number
N_h	number of high-fidelity CFD simulations
N_f	number of low-fidelity CFD simulations
N_{cost}	total design cost
LF	low-fidelity
HF	high-fidelity
CLF	corrected low-fidelity

systems. In mathematical terms, aleatory uncertainties are characterized by probability density functions with sufficient information on the type of the distribution. In order to characterize epistemic uncertainty, probabilistic methods are not suitable due to insufficient information about the uncertainty. One possible approach to model the epistemic uncertainty is to characterize it with intervals. For mixed uncertainty quantification, formulations that combine probabilistic methods and interval approach are usually sought. The aerodynamic response (e.g., the drag coefficient) should be in the form of the combination of probability distribution due to the effect of aleatory input uncertainty and interval distribution which indicate the effect of epistemic uncertainty.

This paper attempts to further reduce the computational cost of the robust design procedure introduced in Zhang et al. [4] and builds upon the recent study by the authors [5], which focused on robust optimization under inherent uncertainties only. The proposed approach is based on replacing the computationally expensive High-Fidelity (HF) CFD model by its inexpensive representation referred to as the Corrected Low-Fidelity (CLF) model. The Low-Fidelity (LF) model is evaluated using the same CFD solver but with a coarser mesh and relaxed convergence criteria. The misalignment between LF and HF models is reduced by means of Output Space Mapping (OSM) [6–9]. The OSM technique has traditionally been used as an auxiliary response correction method in the context of design optimization, with the LF model being corrected at each iteration using the HF model data accumulated during the process. In the proposed approach, the correction can only be performed once, for the points used for constructing the stochastic surrogate model based on Non-Intrusive Polynomial Chaos (NIPC) technique. Moreover, the CLF model has to be aligned sufficiently well with the HF model in the entire design space to be considered in the construction of the surrogate model subsequently utilized in the optimization process. Such an alignment is obtained by using design-variable-dependent multiplicative OSM set up with sufficient number of HF training samples.

In the next section, different robustness measures and objective function formulation for robust design depending on the input uncertainty type are given. The UQ approach, which is the point-collocation NIPC based stochastic expansions is described in Section 3. Further, the multi-fidelity approach involving the construction of the CLF model based on the HF model using OSM strategy is explained in Section 4. To demonstrate the multi-fidelity robust optimization methodology under mixed uncertainties, a CFD example is presented in Section 5 with Mach number considered as aleatory uncertainty and β (geometry) parameter as the epistemic uncertainty. The NACA airfoil shape parameters and the angle of attack are treated as deterministic design variables. Section 6 concludes the paper with important interpretations of the results obtained.

2. Problem formulation for robust optimization

2.1. Deterministic design

In general, the goal of Aerodynamic Shape Optimization (ASO) is to find a shape such that one or more performance metrics are optimized for a given operating condition(s), while at the same time fulfilling a set of constraints. Mathematically, the ASO problem consists of determining values of design variables $\mathbf{x} \in R^n$, such that the objective function $J : R^n \rightarrow R$ is minimized,

$$min \quad J(\mathbf{x}, \mathbf{Q}), \tag{1}$$

subject to constraint equations,

$$\mathbf{g}(\mathbf{x}, \mathbf{Q}) \leq 0, \tag{2}$$

where $\mathbf{Q}$ denotes the vector of conservative flow variables, and $\mathbf{g} : R^n \rightarrow R^m$ is a vector function containing m constraints. The flow variables must satisfy the governing flow equations, $\mathbf{R}$,

$$\mathbf{R}(\mathbf{x}, \mathbf{Q}) = 0. \tag{3}$$

The functions J and $\mathbf{g}$ are assumed to be continuous and differentiable over the design space of interest.

The problem formulation (1)–(3) is general and can be applied to different design approaches. The one-point and one-objective approach is widely adopted, where the aerodynamic surface is optimized for one operating condition with a single merit function. The most common example for this type of optimization is the lift-constrained drag minimization problem. Here, the goal is to improve the aerodynamic efficiency while maintaining a required lift. The objective function is set as

$$J = C_d, \tag{4}$$

where C_d is the drag coefficient and the lift constraint is

$$g = C_l^* - C_l \leq 0, \tag{5}$$

where C_l is the lift coefficient obtained for design $\mathbf{x}$, and C_l^* is the required lift coefficient. Parameters of the operating condition include the Mach number, M_∞, the Reynolds number, Re, and the angle of attack, α (which can be set as a design variable or it can be considered a state variable that is adjusted during the flow solution to satisfy (3)). Formally, we can say that the lift and drag coefficients are a function of the design variables, $\mathbf{x}$, and the state variables, $\mathbf{p} = [M_\infty \; Re \; \alpha]^T$, i.e., $C_d = C_d(\mathbf{x}, \mathbf{p})$ and $C_l = C_l(\mathbf{x}, \mathbf{p})$.

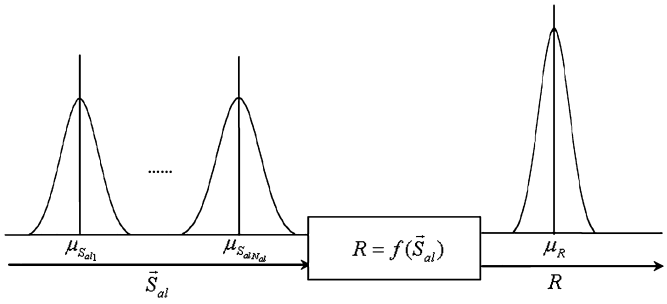

Fig. 1. Robustness estimation of response in presence of aleatory uncertainties.

2.2. Robust design with aleatory uncertainty

Aleatory uncertainty, which is probabilistic and irreducible, describes the inherent variation associated with the physical system (e.g., the operating conditions). Aleatory uncertainties are mathematically characterized by probability density functions when there is enough information on the type of the distribution. In this case, the robustness measure can be based on the mean and the variance (or standard deviation) of the model response. Fig. 1 shows the propagation of input aleatory uncertainties through the simulation code and the uncertainty of the response, $R = f(S_{al})$.

Based on this, the objective for robust aerodynamic design optimization under pure aleatory uncertainty can be formulated as

$$J = \mu_{C_d} + \sigma_{C_d}, \tag{6}$$

where μ_{C_d} is the mean drag coefficient and σ_{C_d} is the standard deviation. The lift constraint can be formulated as

$$g = C_l^* - \mu_{C_l} \leq 0, \tag{7}$$

where μ_{C_l} is the mean lift coefficient.

In the above formulation, the drag and lift coefficients are a function of the deterministic design variable vector $\mathbf{x}$, the deterministic state variable vector p_d and the aleatory input uncertainty vector $\mathbf{S}_{al}$, i.e., $C_d = C_d(\mathbf{x}, \mathbf{p_d}, \mathbf{S}_{al})$ and $C_l = C_l(\mathbf{x}, \mathbf{p_d}, \mathbf{S}_{al})$. The input uncertainty vector is defined as $\mathbf{S}_{al} = (S_{al_1}, S_{al_2}, \ldots, S_{al_{N_{al}}})$ where N_{al} is the number of aleatory uncertainties. Note that, in this case, input uncertainty vector may also contain uncertain state variables such as the free-stream Mach number.

For probabilistic output uncertainty, the mean can be calculated by

$$\mu_{C_d} = E(C_d) = \int_{SR} C_d(\mathbf{x}, \mathbf{p_d}, \mathbf{S}_{al}) P(\mathbf{S}_{al}) d\mathbf{S}_{al}, \tag{8}$$

and the variance as

$$\sigma_{C_d}^2 = E[(C_d - \mu_{C_d})^2] = \int_{SR} (C_d(\mathbf{x}, \mathbf{p_d}, \mathbf{S}_{al}) - \mu_{C_d})^2 P(\mathbf{S}_{al}) d\mathbf{S}_{al}, \tag{9}$$

where $P(\mathbf{S}_{al})$ represents the joint probability function (PDF) of $\mathbf{S}_{al}$ and SR stands for the support region of $\mathbf{S}_{al}$. The mean of the lift coefficient, μ_{C_l}, is calculated in the same way as in Eq. (8).

2.3. Robust design with mixed uncertainty

In real-world engineering systems, both aleatory and epistemic uncertainties exist – called mixed uncertainty. Epistemic uncertainty is reducible and described as lack of knowledge or information in any phase or operation of a design process [3]. For the characterization of epistemic uncertainty, the probabilistic methods are not suitable due to the lack of information about the uncertainty. One approach to model the epistemic uncertainty is to characterize it with intervals. For mixed uncertainty quantification, formulations that combine probabilistic methods and interval approach are sought. When mixed uncertainties exist as input variables, the response R becomes a function of both (aleatory and epistemic) uncertainties, $R = f(S_{al}, S_e)$ as shown in Fig. 2.

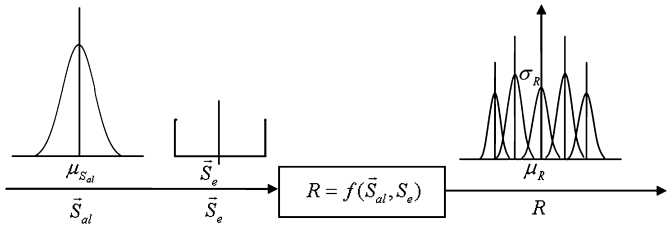

Fig. 2. Robustness estimation of response in presence of mixed uncertainties.

The aerodynamic response should be in form of a combination of the probability distribution due to the effect of aleatory input uncertainty and an interval distribution indicating the effect of epistemic uncertainty. In this case, we have that $C_d = C_d(\mathbf{x}, \mathbf{p_d}, \mathbf{S}_{al}, \mathbf{S}_e)$ and $C_l = C_l(\mathbf{x}, \mathbf{p_d}, \mathbf{S}_{al}, \mathbf{S}_e)$, where $\mathbf{S}_e = (S_{e_1}, S_{e_2}, \ldots, S_{e_{N_e}})$ are the epistemic uncertainties and N_e represents the number of epistemic input uncertainties.

The uncertainty of C_d will consist of infinite number of probability distributions each due to the aleatory input uncertainties at a fixed value of epistemic input uncertainty vector. The intervals at each probability level reflect the effect of epistemic uncertainties on C_d. For the mixed uncertainty case, one approach for the formulation of the objective function can be given as

$$J = w_1 \overline{\mu}_{C_d} + w_2 \overline{\sigma}_{C_d} + w_3 \delta\sigma_{C_d}, \tag{10}$$

where w_i $(i = 1, 2, 3)$ are user-assigned weights, $\overline{\mu}_{C_d}$ denotes mean value of C_d, $\overline{\sigma}_{C_d}$ represents the average standard deviation in C_d, and $\delta\sigma_{C_d}$ denotes the difference between maximum and minimum standard deviations in C_d.

The mean value of C_d will be calculated by

$$\overline{\mu}_{C_d} = \frac{1}{2}(\mu_{C_d}^{max} + \mu_{C_d}^{min}), \tag{11}$$

where $\mu_{C_d}^{max}$ and $\mu_{C_d}^{min}$ are the maximum and minimum means of C_d, respectively. The average value of standard deviation of C_d is obtained by

$$\overline{\sigma}_{C_d} = \frac{1}{2}(\sigma_{C_d}^{max} + \sigma_{C_d}^{min}), \tag{12}$$

where $\sigma_{C_d}^{max}$ and $\sigma_{C_d}^{min}$ are the maximum and minimum standard deviations of C_d, respectively. The difference between the standard deviations of C_d are given by

$$\delta\sigma_{C_d} = \sigma_{C_d}^{max} - \sigma_{C_d}^{min}. \tag{13}$$

The lift constraint can be formulated as

$$g = C_l^* - \overline{\mu}_{C_l} \leq 0. \tag{14}$$

In this study, we use the average standard deviation $\overline{\sigma}_{C_d}$ as a robustness measure for aleatory input uncertainties $\mathbf{S}_{al}$, whereas we utilize the difference in standard deviations $\delta\sigma_{C_d}$ as the robustness measure due to epistemic uncertainties $\mathbf{S}_e$. Both measures will be minimized along with the average C_d using a weighted objective function as given by Eq. (10). The flowchart of robust optimization under mixed uncertainties based on combined stochastic expansions is shown in Fig. 3.

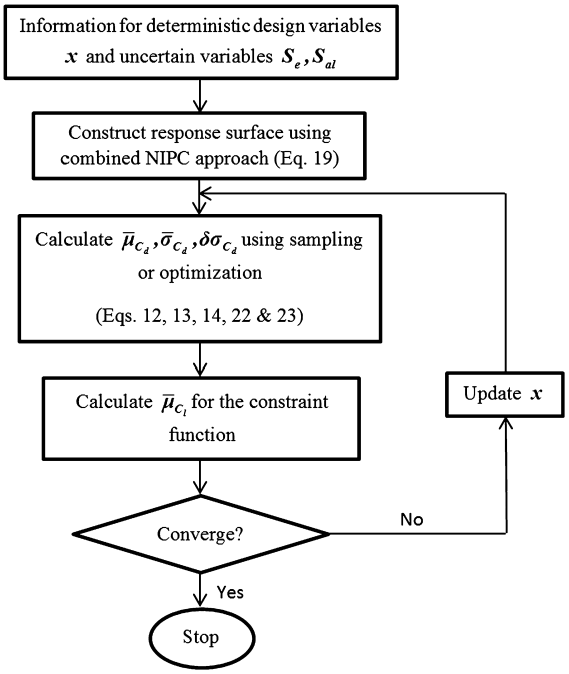

Fig. 3. Flow chart of robust optimization process under mixed uncertainties with combined stochastic expansions.

3. Stochastic expansions for surrogate modeling

For the robust optimization methodology described in this paper, stochastic expansions obtained with the NIPC technique is used due to its computational efficiency and accuracy in uncertainty propagation as shown in the previous studies [10,11]. The stochastic expansions are used as response surfaces (i.e., surrogates of the response) in the optimization procedure and are used to approximate the stochastic objective function and the constraint functions. In the robust optimization problems, we use the point-collocation NIPC approach as explained below.

3.1. Point-collocation non-intrusive polynomial chaos

The point-collocation NIPC is derived from polynomial chaos theory, which is based on the spectral representation of the uncertainty. An important aspect of spectral representation of uncertainty is that one may decompose a random function (or variable) into separable deterministic and stochastic components. For example, for any response variable (i.e., R) in a stochastic optimization problem, one can write:

$$R(\vec{\xi}) \approx \sum_{j=0}^{P} a_j \Psi_j(\vec{\xi}), \tag{15}$$

where a_j is the coefficient of each term in the expansion and $\Psi_j(\vec{\xi})$ is the random basis function corresponding to the jth mode and is a function of n-dimensional random variable vector $\vec{\xi} = (\xi_1, \ldots, \xi_n)$, which has a specific probability distribution. In theory, the polynomial chaos expansion given by Eq. (15) should include infinite number of terms, however in practice a discrete sum is taken over a number of output modes. For a total order expansion, the number of output modes is given by,

$$N_t = P + 1 = \frac{(N+p)!}{N!p!}, \tag{16}$$

which is a function of the order of polynomial chaos (p) and the number of random dimensions (n). The basis function ideally takes the form of multi-dimensional Hermite Polynomial to span the N-dimensional random space when the input uncertainty is Gaussian (unbounded), which was first used by Wiener [12] in his original work of polynomial chaos. To extend the application of the polynomial chaos theory to the propagation of continuous non-normal input uncertainty distributions, Xiu and Karniadakis [13] used a set of polynomials known as the Askey scheme to obtain the "Wiener–Askey Generalized Polynomial Chaos". The Legendre and Laguerre polynomials, which are among the polynomials included in the Askey scheme are optimal basis functions for bounded (uniform) and semi-bounded (exponential) input uncertainty distributions respectively in terms of the convergence of the statistics. An arbitrary polynomial chaos expansion proposed by Witeveen et al. [14] can handle arbitrary distributions of input parameters with limited statistical moments. According to the authors, the Gram–Schmidt orthogonalization algorithm can be used to compute an optimal orthogonal polynomial chaos basis for any type of input distribution. The multivariate basis functions can be obtained from the product of univariate orthogonal polynomials (see Eldred et al. [15]). If the probability distribution of each random variable is different, then the optimal multivariate basis functions can be again obtained by the product of univariate orthogonal polynomials employing the optimal univariate polynomial at each random dimension. This approach requires that the input uncertainties are independent standard random variables, which also allows the calculation of the multivariate weight functions by the product of univariate weight functions associated with the probability distribution at each random dimension. The detailed information on polynomial chaos expansions can be found in Walters and Huyse [16], Najm [17], and Hosder and Walters [18].

To model the uncertainty propagation in computational simulations via polynomial chaos with the intrusive approach, all dependent variables and random parameters in the governing equations are replaced with their polynomial chaos expansions. Taking the inner product of the equations, (or projecting each equation onto jth basis) yields $P+1$ times the number of deterministic equations which can be solved by the same numerical methods applied to the original deterministic system. Although straightforward in theory, an intrusive formulation for complex problems can be relatively difficult, expensive, and time consuming to implement. To overcome such inconveniences associated with the intrusive approach, non-intrusive polynomial chaos formulations have been considered for uncertainty propagation.

The point-collocation NIPC method starts with replacing the uncertain variables of interest with their polynomial expansions given by Eq. (15). Then, $N_t = P + 1$ vectors $(\vec{\xi}_j = \{\xi_1, \xi_2, \ldots, \xi_N\}_j,\ j = 0, 1, \ldots, P)$ are chosen in random space for a given PC expansion with $P+1$ modes and the deterministic code is evaluated at these points. With the left hand side of Eq. (15) known from the solutions of deterministic evaluations at the chosen random points, a linear system of equations can be obtained:

$$\begin{pmatrix} R(\vec{\xi}_0) \\ R(\vec{\xi}_1) \\ \vdots \\ R(\vec{\xi}_P) \end{pmatrix} = \begin{pmatrix} \Psi_0(\vec{\xi}_0) & \Psi_1(\vec{\xi}_0) & \cdots & \Psi_P(\vec{\xi}_0) \\ \Psi_0(\vec{\xi}_1) & \Psi_1(\vec{\xi}_1) & \cdots & \Psi_P(\vec{\xi}_1) \\ \vdots & \vdots & \ddots & \vdots \\ \Psi_0(\vec{\xi}_P) & \Psi_1(\vec{\xi}_P) & \cdots & \Psi_P(\vec{\xi}_P) \end{pmatrix} \begin{pmatrix} a_0 \\ a_1 \\ \vdots \\ a_0 \end{pmatrix}. \tag{17}$$

The coefficients (a_j) of the stochastic expansion are obtained by solving the linear system of equations given above. The solution of the linear problem given by Eq. (17) requires N_t deterministic function evaluations. If more than N_t samples are chosen, then the over-determined system of equations can be solved using the Least Squares approach. Hosder et al. [19] investigated this option on model stochastic problems by increasing the number of collocation points in a systematic way through the introduction of oversampling ratio (n_p) defined as the number of samples divided

by N_t. Based on the study on different model problems, they suggested an effective n_p of 2.0. The point-collocation NIPC has the advantage of flexibility on the selection of collocation points. With the proper selection of collocation points, it has been shown that point-collocation NIPC can produce highly accurate stochastic response surfaces with computational efficiency [19]. In the model problems considered in this study, Latin Hypercube sampling is implemented with an oversampling ratio of 2. The number of response evaluations will be $n_p \times N_t$ when the point-collocation NIPC is used to construct the stochastic response surface.

3.2. Combined NIPC expansion approach

In this work, a combined NIPC expansion approach is used to create the stochastic surrogate model, which will be a function of both the design and the uncertain variables. With the introduction of design variables $\mathbf{x}$, parameters with epistemic uncertainty $\mathbf{S}_e$, and parameters with aleatory uncertainty $\mathbf{S}_{al}$, a combined stochastic expansion of R (i.e., C_d or C_l) based on polynomial chaos can be written as

$$R(\mathbf{S}_{al}(\boldsymbol{\xi}_{sal}), \mathbf{S}_e(\boldsymbol{\xi}_{se}), \mathbf{x}(\boldsymbol{\xi}_d)) = \sum_{j=0}^{P} a_j \Psi_j(\boldsymbol{\xi}_{sal}, \boldsymbol{\xi}_{se}, \boldsymbol{\xi}_d). \tag{18}$$

In this approach, multi-dimensional basis functions Ψ_j are derived from the tensor product of one-dimensional optimum basis functions for the aleatory uncertain variables $\mathbf{S}_{al}$ selected based on the input probability distributions (e.g., Hermite polynomials for normal uncertain variables), the Legendre polynomials (basis) for the epistemic uncertainty variables, and the Legendre polynomials (basis) for the deterministic design variables. The selection of the Legendre polynomials for the epistemic uncertainties and the design variables are due to their bounded nature ($\mathbf{x}_l \le \mathbf{x} \le \mathbf{x}_u$ and $\mathbf{S}_{e,l} \le \mathbf{S}_e \le \mathbf{S}_{e,u}$) and should not be interpreted as a probability assignment to these variables.

In Eq. (18), $\boldsymbol{\xi}_{sal}$ corresponds to a standard aleatory random variable vector, whereas $\boldsymbol{\xi}_{se}$ and $\boldsymbol{\xi}_d$ are the standard variables in interval $[-1, 1]$, which are mapped from the associated intervals of $\mathbf{S}_e$ and $\mathbf{x}$ via

$$\boldsymbol{\xi}_{se} = \left(\mathbf{S}_e - \left(\frac{\mathbf{S}_{e,l} + \mathbf{S}_{e,u}}{2}\right)\right) \Big/ \left(\frac{\mathbf{S}_{e,u} - \mathbf{S}_{e,l}}{2}\right), \tag{19}$$

$$\xi_d = \left(\mathbf{x} - \left(\frac{\mathbf{x}_l + \mathbf{x}_u}{2}\right)\right) \Big/ \left(\frac{\mathbf{x}_u - \mathbf{x}_l}{2}\right). \tag{20}$$

In general, using the combined stochastic expansion and polynomial chaos theory, the mean and variance of R can be calculated by

$$\mu_R(\boldsymbol{\xi}_{se}, \boldsymbol{\xi}_d) = \sum_{j=0}^{P} a_j \left\langle \Psi_j(\boldsymbol{\xi}_{sal}, \boldsymbol{\xi}_{se}, \boldsymbol{\xi}_d) \right\rangle_{\boldsymbol{\xi}_{sal}}, \tag{21}$$

$$\sigma_R^2(\boldsymbol{\xi}_{se}, \boldsymbol{\xi}_d) = \left\{ \sum_{j=0}^{P} \sum_{k=0}^{P} a_j a_k \left\langle \Psi_j\left(\boldsymbol{\xi}_{sal}, \boldsymbol{\xi}_{se}, \boldsymbol{\xi}_d\right) \Psi_k\left(\boldsymbol{\xi}_{sal}, \boldsymbol{\xi}_{se}, \boldsymbol{\xi}_d\right) \right\rangle_{\boldsymbol{\xi}_{sal}} \right\} - \mu_R^2(\boldsymbol{\xi}_{se}, \boldsymbol{\xi}_d), \tag{22}$$

where the inner product expression $\langle .. \rangle$ used in the above equations represent

$$\langle f(\boldsymbol{\xi}) g(\boldsymbol{\xi}) \rangle_{\boldsymbol{\xi}} = \int_{SR} f(\boldsymbol{\xi}) g(\boldsymbol{\xi}) p(\boldsymbol{\xi}) d\boldsymbol{\xi}, \tag{23}$$

written in terms of two generic functions $f(\boldsymbol{\xi})$ and $g(\boldsymbol{\xi})$ in the support region SR of $\boldsymbol{\xi}$ with $p(\boldsymbol{\xi})$ being the weight function. Note that when the design variables are not considered as uncertain (as the case studied in this paper), the surrogates need not to be recreated at every optimization iteration. In this case one can directly compute the output statistics (mean, standard deviation and variance) by using a single stochastic response surface created for the response quantity of interest (i.e., C_d and C_l)

4. Multi-fidelity modeling approach

The robust design formulations described in Section 2 are desired to be obtained using a HF CFD model. However, accurate CFD models are computationally expensive and if the design space is large, the computational cost can be prohibitive. Therefore, to reduce the computational effort, a multi-fidelity approach is considered. In this process, the HF CFD model is replaced by a CLF model. In the following sections, we describe the HF CFD model, LF CFD model and the CLF model construction using space mapping method.

4.1. High-fidelity CFD model

The robust design under mixed uncertainty is demonstrated for the drag minimization of NACA 4-digit airfoils described with three geometric design variables over the range of uncertainties at transonic flow conditions. The deterministic CFD simulations were performed with the FLUENT [20] code to solve steady, 2-D, compressible, turbulent RANS equations. The fluid medium is air, assumed to be an ideal gas, with the laminar dynamic viscosity (μ) described by Sutherland's formula [21].

For modeling the turbulent kinematic eddy viscosity (ν_t), we use the turbulence model by Spalart and Allmaras [22]. The Spalart–Allmaras model, designed specifically for aerodynamic wall-bounded flows, is a one-equation model that solves a single conservation partial differential equation for the turbulent viscosity. This conservation equation contains convective and diffusive transport terms, as well as expressions for the production and dissipation of ν_t. The Spalart–Allmaras model is economical and accurate for attached wall-bounded flows, and flows with mild separation and recirculation.

The solution domain boundaries are placed at 25 chord lengths in front, below and above the airfoil with front to wake ratio of one. An example computational grid along with a typical airfoil section is shown in Fig. 4. A hyperbolic grid generator [23] is used for the mesh generation. The non-dimensional normal distance (y^+) from the wall to the first grid point is roughly one. The free-stream Mach number, angle of attack, static pressure, and the turbulent viscosity ratio are prescribed at the farfield boundary. A grid convergence study is performed using the NACA 2412 airfoil at Mach number $M = 0.75$ and angle of attack $\alpha = 1°$. The study revealed that a grid level of approximately 510,000 cells are needed for mesh convergence, which is treated as the HF model for the current study.

The flow solver utilizes implicit density-based formulation and the fluxes are calculated by an upwind-biased second-order spatially accurate Roe flux scheme. Asymptotic convergence to a steady state solution is obtained for each case. Automatic solution steering is employed to gradually ramp up the Courant number and accelerate convergence. Full multi-grid initialization is used to accelerate the iterative convergence. The iterative convergence of each solution is examined by monitoring the overall residuals, which is the sum (over all the cells in the computational domain) of the L^2 norm of all the governing equations solved in each cell. In addition to this, the lift and drag forces are monitored for convergence. The solution convergence criterion for the CFD runs is a reduction in the residuals by six orders of magnitude.

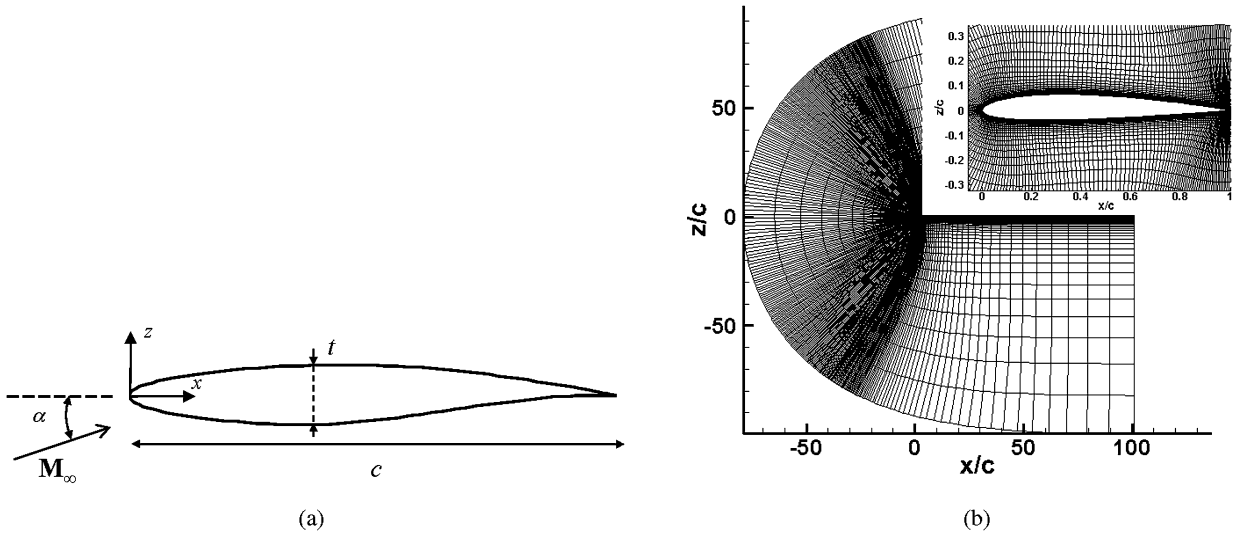

Fig. 4. (a) A typical airfoil section is shown. The free-stream flow is at Mach number M_∞ and at an angle of attack α relative to the chord axis. (b) An example computational grid.

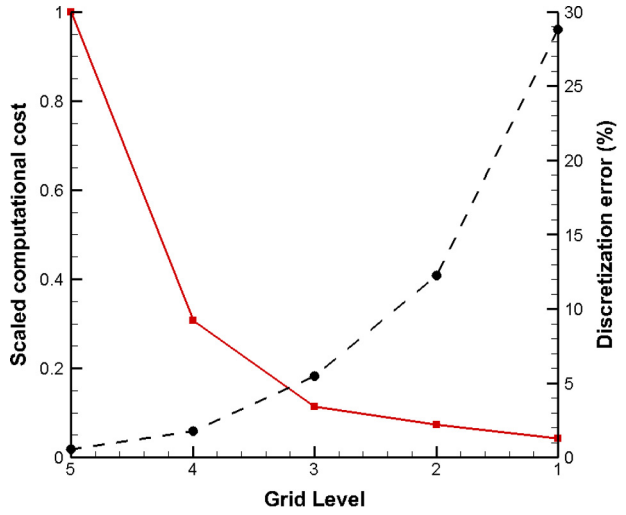

Fig. 5. Computational cost comparison for different grid levels (left Y-axis) and grid convergence in terms of Discretization Error (DE) for C_d (right Y-axis).

4.2. Low-fidelity CFD model

The LF CFD model is constructed with the same solution and physical modeling parameters as the HF model, but with a coarser computational mesh. In the determination of the LF model, we have studied 5 grid levels (Table 1). The grid levels affect the magnitude of the discretization error as it determines the spatial resolution. Richardson extrapolation [24] technique has been used to estimate the magnitude of the discretization error for C_d at each grid level and the results are summarized in Fig. 5. In this work, two case studies are presented in terms of LF CFD models. Grid levels 2 and 3 solutions are treated as the low-fidelity models and the results are compared with the HF model, after correction.

The computational resources for all CFD simulations consisted of 3 processors with a CPU speed of 2.66 GHz. The ratio of simulation times (in seconds) of the high- and low-fidelity models (for grid level 2 and 3) is around 14 and 9 respectively. Fig. 5 also compares the computational cost of the high- and low-fidelity models in terms of simulation time (in seconds) scaled with respect to the HF model.

Table 1
Mesh size nomenclature and discretization error results for C_d.

Grid level	Mesh size	Cells	DE (%)
1	99×20	1980	28.83
2	199×40	7960	12.23
3	399×80	31 920	5.49
4	799×160	127 840	1.75
5	1599×320	511 680	0.56

4.3. Corrected low-fidelity model construction using output space mapping

To reduce the computational cost of the design process, the HF CFD model is replaced by a suitably corrected low-fidelity one, the latter being evaluated using the same CFD solver but with a coarser mesh. In specific, the model correction is implemented to the LF CFD sample points (solutions) utilized for the construction of stochastic surrogate based on NIPC by using Output Space Mapping (OSM) technique. The OSM correction can be obtained without costly parameter extraction procedure and ensures that the low-fidelity model represents the high-fidelity one with sufficient accuracy. The correction procedure can be outlined as follows: Define vector $\mathbf{x_c} = [\mathbf{x}\ S_{al}\ S_e]^T$ and let the HF model response be $h(\mathbf{x_c}) = [C_{l.h}(\mathbf{x_c})\ C_{d.h}(\mathbf{x_c})]^T$, where $C_{l.h}$ and $C_{d.h}$ are (high-fidelity CFD-simulated) lift and drag coefficients. Similarly, the LF model response is $f(\mathbf{x_c}) = [C_{l.f}(\mathbf{x_c})\ C_{d.f}(\mathbf{x_c})]^T$. The CLF model is denoted as $c(\mathbf{x_c}) = [C_{l.c}(\mathbf{x_c})\ C_{d.c}(\mathbf{x_c})]^T$.

In space mapping, the corrected model is a composition of the low-fidelity model and simple, usually linear, transformations (or mappings) [6]. In this work, the correction terms are directly applied to the response components $C_{l.f}(\mathbf{x_c})$ and $C_{d.f}(\mathbf{x_c})$ of the low-fidelity model. The corrected model is defined as:

$$c(\mathbf{x_c}) = \mathbf{A}(\mathbf{x_c}) \circ f(\mathbf{x_c}) + \mathbf{D} = [a_l(\mathbf{x_c})C_{l.f}(\mathbf{x_c}) + d_l \quad a_d(\mathbf{x_c})C_{d.f}(\mathbf{x_c}) + d_d]^T, \tag{24}$$

where $\circ$ denotes a component-wise multiplication. The multiplicative correction term is design-variable-dependent and takes the form of

$$\mathbf{A}(\mathbf{x_c}) = [a_{l.0} + [a_{l.1}\, a_{l.2}\, \ldots\, a_{l.n}] \cdot (\mathbf{x_c} - \mathbf{x_c}^0)a_{d.0} + [a_{d.1}\, a_{d.2}\, \ldots\, a_{d.n}] \cdot (\mathbf{x_c} - \mathbf{x_c}^0)]^T, \tag{25}$$

where $\mathbf{x_c}^0$ is the center of the design space. Response correction parameters $\mathbf{A}$ and $\mathbf{D}$ are obtained as

$$[\mathbf{A}, \mathbf{D}] = \arg\min_{\bar{\mathbf{A}},\bar{\mathbf{D}}} \sum_{k=1}^{K} ||h(\mathbf{x_c}^k) - (\bar{\mathbf{A}}(\mathbf{x_c}^k) \circ f(\mathbf{x_c}^k) + \bar{\mathbf{D}})||^2, \tag{26}$$

i.e., the response scaling is supposed to (globally) improve the matching for all training points $\mathbf{x_c}^k$, $k = 1, \ldots, K$. $2n+1$ training points (n being the number of design variables) are chosen for correcting the LF model. The correction parameters $\mathbf{A}$ and $\mathbf{D}$ can be calculated analytically as follows

$$\begin{bmatrix} a_{l.0} \\ a_{l.1} \\ \vdots \\ a_{l.n} \\ d_l \end{bmatrix} = \left(\mathbf{C}_l^T \mathbf{C}_l\right)^{-1} \mathbf{C}_l^T \mathbf{F}_l, \quad \begin{bmatrix} a_{d.0} \\ a_{d.1} \\ \vdots \\ a_{d.n} \\ d_d \end{bmatrix} = \left(\mathbf{C}_d^T \mathbf{C}_d\right)^{-1} \mathbf{C}_d^T \mathbf{F}_d\,, \tag{27}$$

$$\mathbf{C}_l = \begin{bmatrix} C_{l.f}(\mathbf{x_c}^1) & C_{l.f}(\mathbf{x_c}^1)\cdot(\mathbf{x_c}_1^1 - \mathbf{x_c}_1^0) & \cdots & C_{l.f}(\mathbf{x_c}^1)\cdot(\mathbf{x_c}_n^1 - \mathbf{x_c}_n^0) & 1 \\ C_{l.f}(\mathbf{x_c}^2) & C_{l.f}(\mathbf{x_c}^2)\cdot(\mathbf{x_c}_1^2 - \mathbf{x_c}_1^0) & \cdots & C_{l.f}(\mathbf{x_c}^2)\cdot(\mathbf{x_c}_n^2 - \mathbf{x_c}_n^0) & 1 \\ \vdots & \vdots & \ddots & \vdots & \vdots \\ C_{l.f}(\mathbf{x_c}^K) & C_{l.f}(\mathbf{x_c}^K)\cdot(\mathbf{x_c}_1^K - \mathbf{x_c}_1^0) & \cdots & C_{l.f}(\mathbf{x_c}^K)\cdot(\mathbf{x_c}_n^K - \mathbf{x_c}_n^0) & 1 \end{bmatrix}, \tag{28}$$

$$\mathbf{F}_l = \begin{bmatrix} C_{l.h}(\mathbf{x_c}^1) & C_{l.h}(\mathbf{x_c}^2) & \cdots & C_{l.h}(\mathbf{x_c}^K) \end{bmatrix}^T, \tag{29}$$

$$\mathbf{C}_d = \begin{bmatrix} C_{d.f}(\mathbf{x_c}^1) & C_{d.f}(\mathbf{x_c}^1)\cdot(\mathbf{x_c}_1^1 - \mathbf{x_c}_1^0) & \cdots & C_{d.f}(\mathbf{x_c}^1)\cdot(\mathbf{x_c}_n^1 - \mathbf{x_c}_n^0) & 1 \\ C_{d.f}(\mathbf{x_c}^2) & C_{d.f}(\mathbf{x_c}^2)\cdot(\mathbf{x_c}_1^2 - \mathbf{x_c}_1^0) & \cdots & C_{d.f}(\mathbf{x_c}^2)\cdot(\mathbf{x_c}_n^2 - \mathbf{x_c}_n^0) & 1 \\ \vdots & \vdots & \ddots & \vdots & \vdots \\ C_{d.f}(\mathbf{x_c}^K) & C_{d.f}(\mathbf{x_c}^K)\cdot(\mathbf{x_c}_1^K - \mathbf{x_c}_1^0) & \cdots & C_{d.f}(\mathbf{x_c}^K)\cdot(\mathbf{x_c}_n^K - \mathbf{x_c}_n^0) & 1 \end{bmatrix}, \tag{30}$$

$$\mathbf{F}_d = \begin{bmatrix} C_{d.h}(\mathbf{x_c}^1) & C_{d.h}(\mathbf{x_c}^2) & \cdots & C_{d.h}(\mathbf{x_c}^K) \end{bmatrix}^T, \tag{31}$$

which is a least-square optimal solution to the linear regression problems $\mathbf{C}_l\,[a_{l.0}\ a_{l.1}\ \ldots\ a_{l.n}\ d_l]^T = \mathbf{F}_l$ and $\mathbf{C}_d\,[a_{d.0}\ a_{d.1}\ \ldots\ a_{d.n}\ d_d]^T = \mathbf{F}_d$, equivalent to (26). Note that the matrices $\mathbf{C}_l^T\mathbf{C}_l$ and $\mathbf{C}_d^T\mathbf{C}_d$ are non-singular for $K > n+1$, which is the case for our choice of the training set.

5. Demonstration example

In this section, the multi-fidelity robust design approach is demonstrated on an airfoil shape optimization problem under mixed uncertainty. In particular, the accuracy and optimization cost of the proposed approach is compared with the cost of using directly the high-fidelity CFD model for creating stochastic surrogate.

5.1. Formulation and setup

The robust airfoil optimization under mixed uncertainty is formulated as

$$\begin{aligned} &\textit{min} \quad w_1\bar{\mu}_{C_d} + w_2\bar{\sigma}_{C_d} + w_3\delta\sigma_{C_d}, \\ &\textit{subject to} \quad C_l^* - \bar{\mu}_{C_l} \le 0, \\ &0.005 \le m \le 0.05, \\ &0.3 \le p \le 0.7, \\ &0.08 \le t/c \le 0.14, \\ &0.5 \le \alpha \le 1.5, \end{aligned} \tag{32}$$

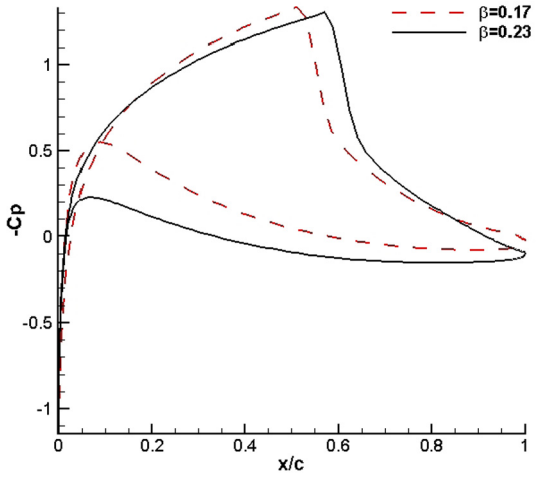

Fig. 6. Pressure distribution for NACA 2412 at $M = 0.75$, $\alpha = 1°$.

where the profile drag coefficient ($C_d = C_d(\mathbf{x}, \mathbf{S}_{al}, \mathbf{S}_e)$) and the lift coefficient ($C_l = C_l(\mathbf{x}, \mathbf{S}_{al}, \mathbf{S}_e)$) are a function of deterministic design variable vector $\mathbf{x} = \{m, p, t/c, \alpha\}$, aleatory input uncertainty vector $\mathbf{S}_{al}$ and the epistemic input uncertainty vector $\mathbf{S}_e$. In particular, the NACA 4-digit parameterization method is used where the airfoil shape is defined by three parameters: m (the maximum ordinate of the mean camber line as a fraction of chord), p (the chordwise position of the maximum ordinate as a fraction of chord) and t/c (thickness-to-chord ratio). The NACA 4-digit parameterization is explained in detail by Abbott and Doenhoff [25].

The free-stream Mach number is treated as a normally distributed aleatory (inherent) input uncertainty ($\mathbf{S}_{al} = \{M\}$) with a mean value $\mu = 0.75$ and standard deviation $\sigma = 0.015$. The equation for a modified symmetrical 4-digit NACA airfoil is given by Eq. (33):

$$y_t = \frac{t}{\beta}\left[0.2969\sqrt{\frac{x}{c}} - 0.1260\frac{x}{c} - 0.3516\frac{x^2}{c} + 0.2843\frac{x^3}{c} - 0.1036\frac{x^4}{c}\right]. \tag{33}$$

The geometry parameter β (default value of 0.2 in the nominal equation) is modeled as an epistemic input uncertainty (i.e., $\mathbf{S}_e = \{\beta\}$) with bounds $[0.17, 0.23]$. The range of β is chosen to mimic the epistemic uncertainty in the thickness distribution formula defining the shape of the airfoil. Fig. 6 shows the pressure distributions of NACA 2412 airfoil at $M = 0.75$ and $\alpha = 1°$ for two β values corresponding to the limits of the epistemic interval. It can be seen that the β parameter has considerable effect on the pressure distribution including the shock location. In the optimization formulation, the mean lift coefficient limit is set to $C_l^* = 0.55$. The formulation also includes geometric constraints for the profile shape, which bound the maximum camber, maximum camber location and the thickness. In this study, equal weights ($w_1, w_2, w_3 = 1$) are assigned to each term in the objective function for demonstration purposes, however one can choose different values depending on the emphasis on each term. Besides the selection of different weights, it is also possible to normalize each term in Eq. (10) with the statistics obtained from a reference design (e.g., initial design) to control the dominancy of each term in the objective function.

5.2. Stochastic response surface (surrogate model)

The robust optimization approach is based on stochastic expansions derived from the NIPC technique, which are used as surro-

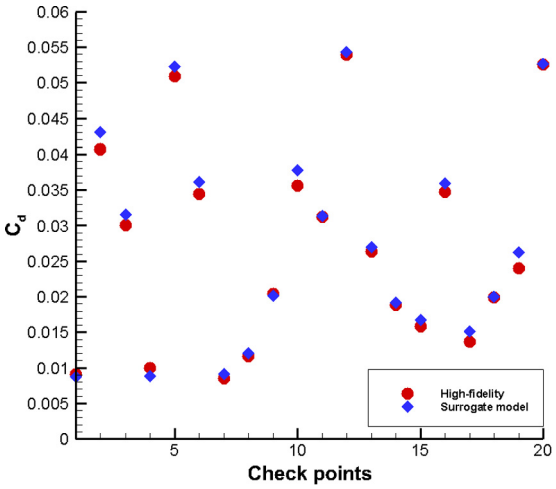

Fig. 7. NIPC Response surface accuracy at 20 LH sample points within the domain.

gates in the optimization process. The combined expansion approach (see Section 3.2) used in this study makes the optimization process very efficient, since a single response surface is created as a function of both design variables and the uncertain variables. It should be noted that the combined expansion approach will be ideal for problems with fewer number of design and uncertain variables (e.g., $N_d \leq 4$ and $N_p \leq 2$). On the other hand, in optimization problems with large number of design variables, one can choose an alternative approach which is based on the expansion of polynomial chaos surface only on the uncertain (aleatory and epistemic) variables. With this approach a separate stochastic response surface should be created at each design point, which will increase the computational cost, however the accuracy of the response surface approximation will increase due to the reduction in the number of expansion variables.

For this particular study, a 3rd order polynomial chaos expansion is implemented with an oversampling ratio of 2, which required a total number of 168 CFD evaluations to create the response surface. In addition to the high-fidelity CFD model (grid level 5, Section 4.1), the stochastic response surfaces were also created with two low-fidelity models (grid level 2 and grid level 3, Section 4.2) and the corrected low-fidelity models (Section 4.3) to evaluate the results of the multi-fidelity approach. In order to check the accuracy of each response surface, the coefficient of drag is compared to that of CFD simulations at the same fidelity level at 20 Latin Hypercube (LH) samples chosen in the design and uncertainty space. Fig. 7 demonstrates the accuracy of the surrogate model created with the high-fidelity CFD model (i.e., grid level 5) with a Root Mean Square Percentage Error (RMSPE) of 4.94% in C_d values, evaluated using Eqs. (34) and (35).

$$\text{Percentage Error (PE)} = \frac{(C_d^{CFD} - C_d^{NIPC})}{C_d^{CFD}} \times 100, \tag{34}$$

$$\text{Root Mean Square PE} = \sqrt{\frac{\sum_{i=1}^{n_{chk}} PE_i^2}{n_{chk}}}, \tag{35}$$

where n_{chk} represents the number of check points which is 20 in this case.

After the creation of stochastic response surfaces, the robust optimization is performed with the procedure described in Section 2.3 and outlined in Fig. 3. For the non-linear constraint optimization, sequential least squares quadratic programming algorithm is implemented.

5.3. Optimization results and discussion

The objective of the optimization formulation is to reduce the average of the mean ($\overline{\mu}_{C_d}$), average standard deviation ($\overline{\sigma}_{C_d}$) and the difference in standard deviation of the drag coefficient ($\delta\sigma_{C_d}$) simultaneously in order to obtain an airfoil shape with minimum drag that is least sensitive to the change in Mach number M and the β parameter over the uncertainty range specified for each variable. Besides the geometric constraints on design variables, the optimization is performed such that the mean lift coefficient is greater than or equal to 0.55.

5.3.1. Accuracy of the corrected low-fidelity model

To demonstrate the multi-fidelity approach, the robust optimization is performed on the surrogates created by the following two CLF models with the OSM technique:

- CLF (grid level 2): OSM applied to grid level 2 as LF model (HF model: grid level 5)
- CLF (grid level 3): OSM applied to grid level 3 as LF model (HF model: grid level 5)

The stochastic response surfaces for drag and lift coefficients are created for the HF CFD model, LF CFD models and the CLF responses (i.e., CLF grid level 2 and CLF grid level 3). The optimization was performed starting with an initial airfoil geometry of NACA 2412. As can be seen from Table 2, the optimization runs converged to similar optimum airfoil shapes in terms of location of maximum camber ($p = 0.7$, the design variable upper bound) and the thickness ($t/c = 0.08$, the design variable lower bound). The maximum camber slightly varies for the LF and CLF models as compared to the HF model. One of the reasons for similar designs using a low-fidelity model is that the flow field around the optimal airfoil shape does not include complex flow features such as strong shocks and shock induced separation over the range of uncertain parameters, making it possible to capture the flow behavior using a lower grid resolution. Another reason is the relatively low number of design variables (i.e., shape parametrization variables) defining the NACA 4-digit airfoil, which allow only a limited number of designs to evaluate.

Although the optimized designs are comparatively similar, the difference can be attributed to the LF and HF models in terms of accuracy or convergence of statistics (for, e.g., $\overline{\mu}_{C_d}$, σ_{C_d}, etc.). Fig. 8(a) provides a summary of results for the average of the mean of the drag coefficient ($\overline{\mu}_{C_d}$) for the optimized design with varying target lift coefficient values (C_l^*). It can be inferred that the convergence of the LF model for grid levels 2 and 3 are inaccurate in terms of $\overline{\mu}_{C_d}$, the most dominant term in the objective function. The CLF model for grid level 2 does show improvement as compared to its corresponding LF model. However, the CLF model for grid level 3 approximates the HF model with considerable accuracy. For example, the $\overline{\mu}_{C_d}$ of LF model for grid levels 2 and 3 for a target lift coefficient of 0.4 are 74.5 and 64 drag counts respectively. After the correction is applied to the LF models, the optimization process converges to 65 drag counts for CLF grid level 2 and 62 drag counts for CLF grid level 3 which exactly matches with the HF model. This behavior is expected as the grid level 3 has 32,000 mesh cells as compared to only 8000 mesh cells for grid level 2, which corresponds to less noise and better grid resolution.

Fig. 8(b) represents the probability box (p-box) for C_d over the uncertainty range of the Mach number (M) and the β parameter for the optimized airfoil design at a target lift coefficient $C_l^* = 0.55$. Similar to previous results, the LF model for grid level 2 inaccurately represents the uncertainty in C_d as compared to the HF model. In contrast, the difference between the HF model and the

Table 2
Optimization results using the stochastic surrogates created with the low-fidelity (LF), high-fidelity (HF) and the corrected low-fidelity (CLF) models.

Variable	LF (Grid level 2)	LF (Grid level 3)	CLF (Grid level 2)	CLF (Grid level 3)	HF model
m	0.0189	0.0198	0.0193	0.0196	0.0195
p	0.7	0.7	0.7	0.7	0.7
t/c	0.08	0.08	0.08	0.08	0.08
α	0.5	0.5	0.5	0.5	0.5
$\overline{\mu}_{C_l}$	0.55	0.55	0.55	0.5499	0.55
$\overline{\mu}_{C_d}$	78	69	71.17	67.42	66.618
σ_{C_d}	12.6	12.9	17.26	14.99	13.55
$\delta\sigma_{C_d}$	10.7	10.5	13.301	9.268	9.523
N_f	168	168	181	181	0
N_h	0	0	13	13	168
N_{cost}	12	19	26	34	168

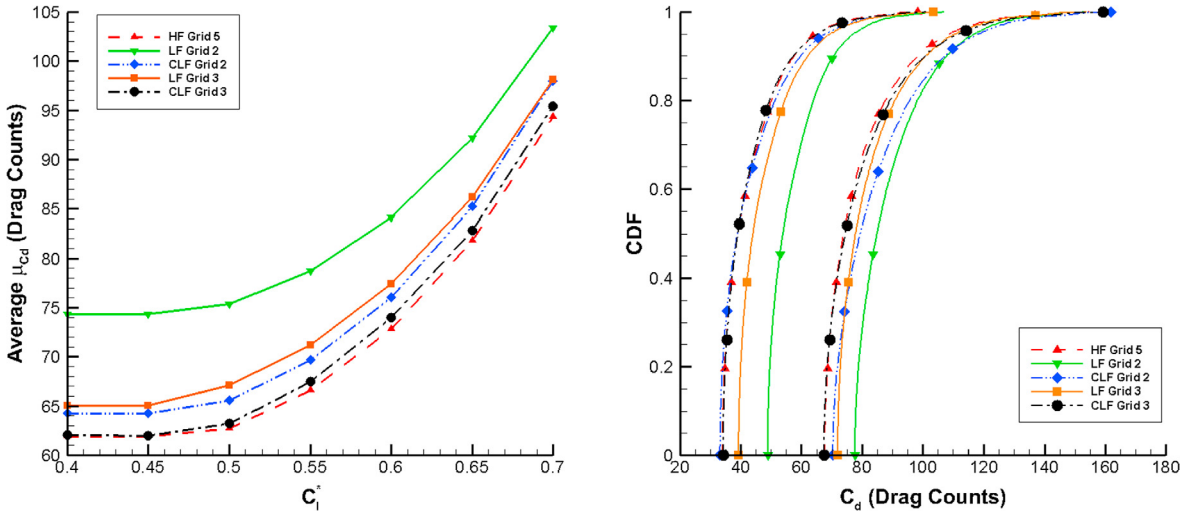

(a) (b)

Fig. 8. (a) Average mean C_d for varying target lift coefficients, C_l^*. (b) Probability box for C_d at a target lift coefficient of 0.55.

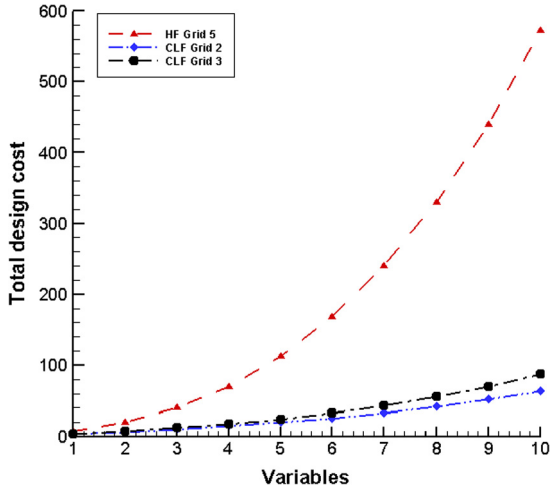

Fig. 9. The total design cost versus the number of variables (design + uncertain variables) for optimization with different models.

CLF model for grid level 3 is minimal. The 95% confidence interval (CI) for the LF model using grid level 2 and grid level 3 are [48.90, 124.83] and [39.32, 119.80] drag counts respectively. Similarly, the 95% CI for CLF model using grid level 2 and grid level 3 are [33.20, 127.80] and [33.22, 120.67] drag counts respectively, as compared to [33.94, 118.33] drag counts for the HF model. As explained previously, the OSM correction can be obtained without costly parameter extraction procedure and ensures that the CLF model represents the HF model with sufficient accuracy (CLF grid level 3 in this study).

In terms of computational cost, there is a large difference between the direct HF and the multi-fidelity approach. The total computational cost (N_{cost}) of optimization varies with the number of expansion variables by a power of 3 (polynomial order 3 is used in this study), in case of using the HF model directly to create the surrogate. For the current study, as the over-sampling ratio is 2, the total cost corresponds to $n_p \times N_t = (n^3 + 6n^2 + 11n + 6)/3$. The total computational cost of optimization using the multi-fidelity approach is the sum of cost of the HF model evaluations (N_h) and LF model evaluations (N_f). The HF model is sampled $N_h = 2n + 1$ times and the LF model is sampled $N_f = n_p \times N_t + (2n + 1) = (n^3 + 6n^2 + 17n + 9)/3$. The overall cost of the multi-fidelity approach in terms of equivalent HF model evaluations can be given by $N_{cost} = N_h + N_f/r$, where r is the ratio of HF to LF simulation times. As can be seen from Table 2, the total cost of using the HF model directly is 168 HF simulations, whereas the multi-fidelity (CLF grid level 3) approach requires 181 LF model evaluations and 13 HF model evaluations, corresponding to a total cost of 34 equivalent HF model evaluations. Further, a comparison of the design cost for the HF model and the CLF model is shown in Fig. 9 up to a variable number of 10, which may include both the design variables and the uncertain parameters.

5.3.2. Robustness for the optimized design

Fig. 10 presents the optimization results (uncertainty for the optimized airfoil as compared to the initial airfoil design) and the convergence history of average mean ($\overline{\mu}_{C_d}$, see Fig. 10(b)), aver-

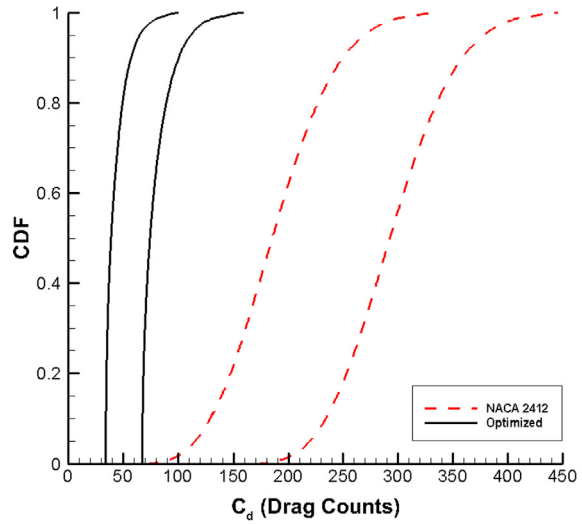

(a) Probability box for C_d

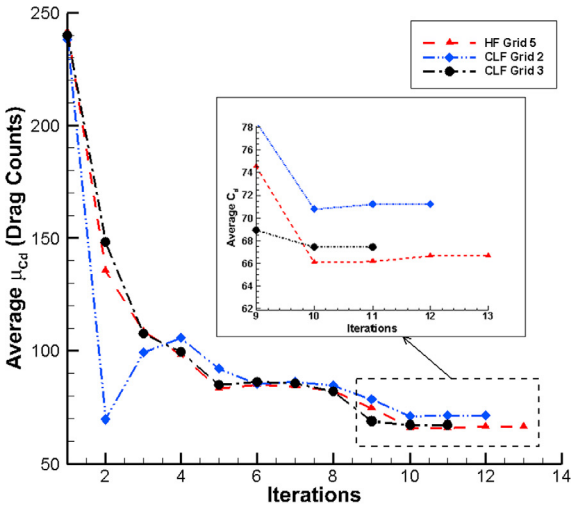

(b) Average mean of C_d, $\overline{\mu}_{C_d}$

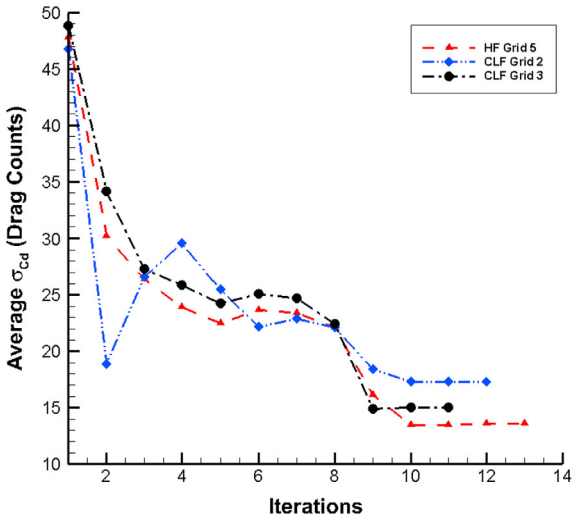

(c) Average standard deviation of C_d, $\overline{\sigma}_{C_d}$

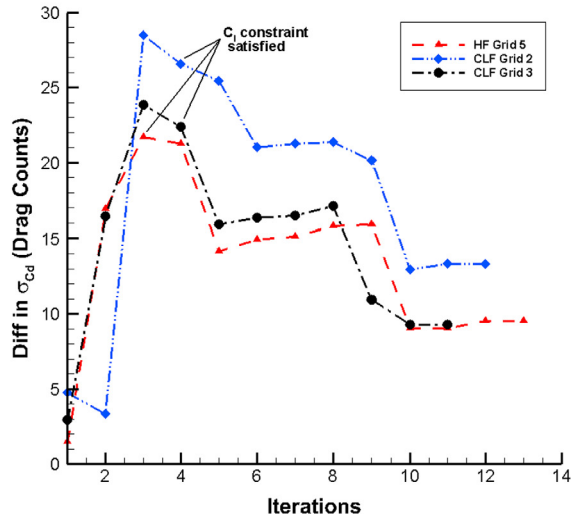

(d) Difference in standard deviation of C_d, $\delta\sigma_{C_d}$

Fig. 10. The optimization history for different terms in the objective function under mixed uncertainty with an initial airfoil geometry of NACA 2412 with $C_l^* = 0.55$.

age standard deviation ($\overline{\sigma}_{C_d}$, see Fig. 10(c)) and the difference in standard deviation ($\delta\sigma_{C_d}$, see Fig. 10(d)) for a target lift coefficient of 0.55. The results correspond to an initial airfoil shape of NACA 2412 being optimized for robustness under mixed uncertainty. The p-box plot in Fig. 10(a) demonstrates the robustness of the optimized design as compared to the initial design.

In specific, along with the average mean for C_d, the average standard deviation (robustness in terms of aleatory uncertainty) and the difference in standard deviation that defines the width of the p-box plot (robustness in terms of epistemic uncertainty) is also reduced simultaneously. All three quantities are reduced as compared to their starting values but the converged value is different for different models (HF and CLF). CLF using grid level 3 is a better approximation for the HF model in terms of all three quantities. The reduction in the average mean of C_d is the highest in terms of drag counts, followed by the average standard deviation and the difference in standard deviation for C_d. This is due to the fact that the average of the mean of C_d is the most dominant term in the objective function. One may also expect different convergence statistics if different weights are assigned to each term. Alternatively, the difference in standard deviation increases as compared to the initial design. However, an important point to note is that the C_l constraint is satisfied at the 3rd and 4th iterations for the HF and CLF models respectively. Thereafter, the $\delta\sigma_{C_d}$ quantity reduces and converges to its optimum value.

Fig. 11 shows the surface plot of the drag coefficient over the range of Mach number (M) and the β parameter. Both CLF models (CLF grid level 2 and 3) verify that the aerodynamic characteristics for the optimum airfoil are better as compared to the characteristics of NACA 2412. However, even in this case, the CLF using grid level 3 outperforms the one using grid level 2 in terms of accuracy with respect to the HF model. The results show that there is a significant drag rise for the CLF model using grid level 2 at high Mach numbers and lower β values. On the other hand, the drag coefficients for CLF model using grid level 3 are in good agreement with the HF model.

5.3.3. *Optimization using different initial airfoils*

To ensure that the optimization process does not converge to a local minimum, different initial airfoil designs have been implemented. Along with NACA 2412 as the initial airfoil shape,

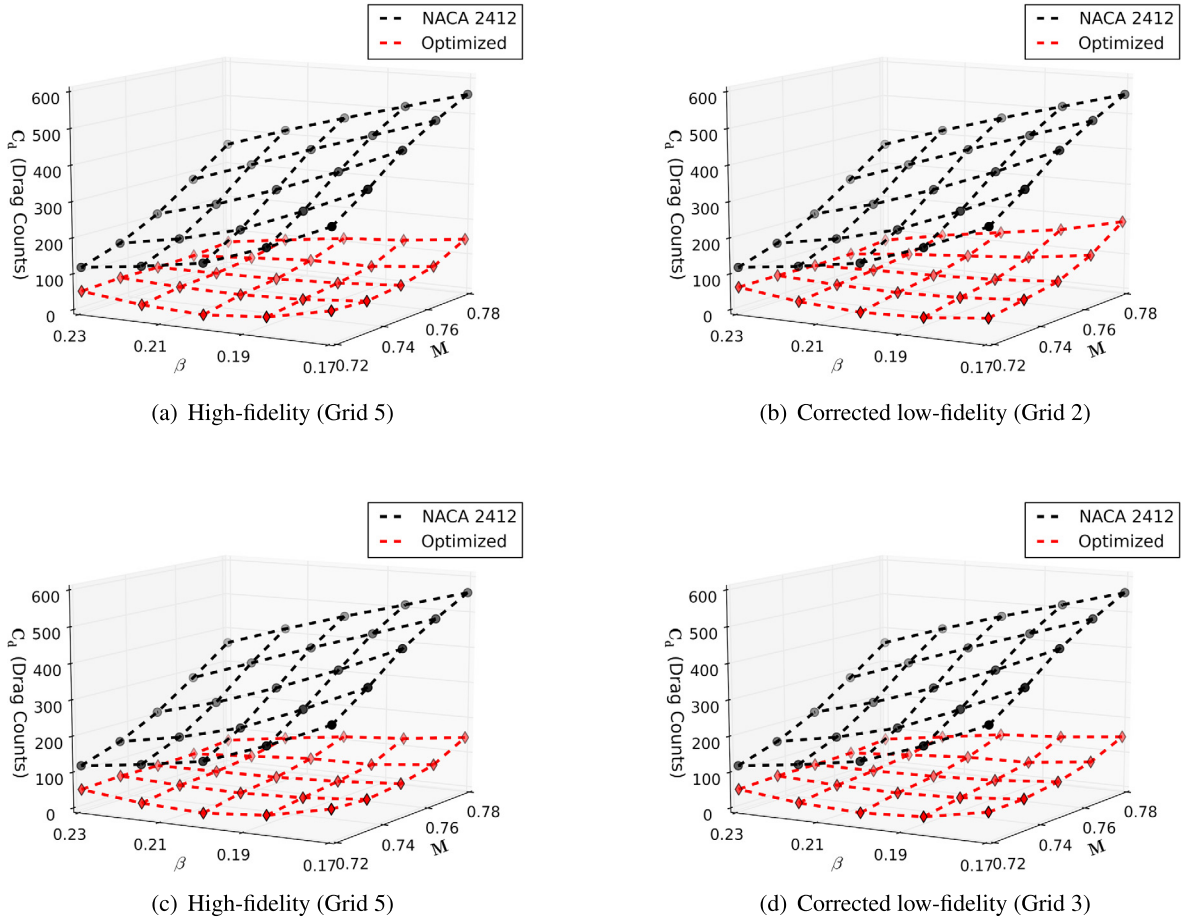

(a) High-fidelity (Grid 5)

(b) Corrected low-fidelity (Grid 2)

(c) High-fidelity (Grid 5)

(d) Corrected low-fidelity (Grid 3)

Fig. 11. Drag coefficient values of the optimized airfoil and NACA 2412 for varying Mach number (M) and β parameter.

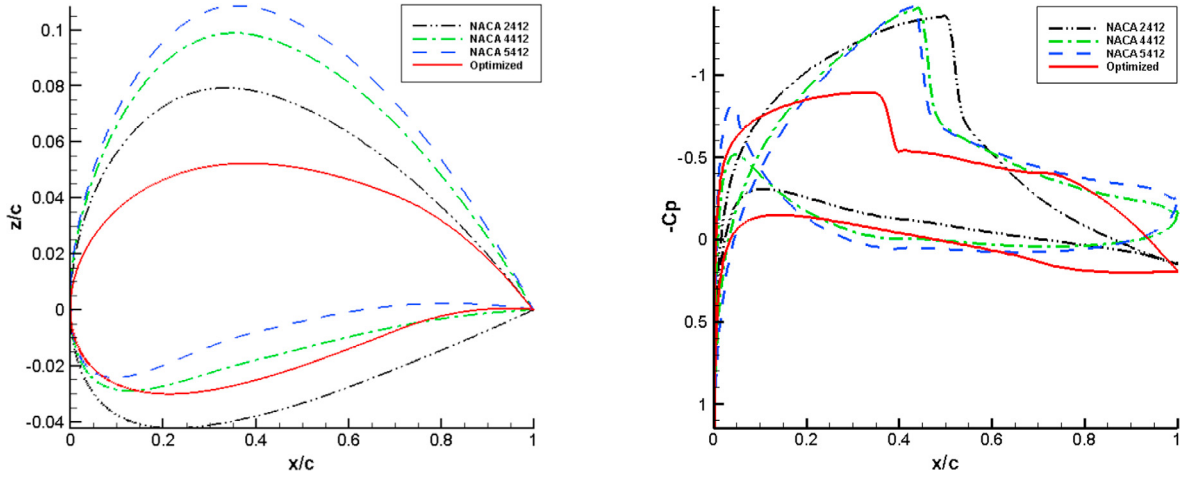

(a)

(b)

Fig. 12. Characteristics of the initial and optimized airfoils: (a) initial and optimized airfoil shapes, and (b) pressure coefficient plot at a lift coefficient of 0.55.

NACA 4412 and NACA 5412 have been tested as initial airfoils with the same formulation and setup for the robust optimization as mentioned in Section 5.1. The mean lift coefficient limit is set to $C_l^* = 0.55$. Fig. 12(a) compares the initial airfoil designs with the optimum airfoil shape corresponding to CLF model using grid level 3. The pressure coefficient plot is also compared for all the initial airfoil designs with the optimum airfoil in Fig. 12(b). At a free-stream Mach number $M = 0.75$ and $\beta = 0.2$, all the initial airfoil designs have a strong shock on the top surface, whereas the strength of the shock is reduced considerably on the optimized airfoil. This is mainly due to the increase in minimum suction pressure and reduction in the maximum velocity on the top surface of the optimized airfoil. The aft camber compensates for the loss in lift in the suction region. Furthermore, the Mach and pressure contours for the optimized airfoil design are compared to NACA 2412 (one of the initial airfoil designs) in Fig. 13. The reduced shock strength and elimination of the shock induced flow separation over the optimized airfoil geometry can also be observed in this figure.

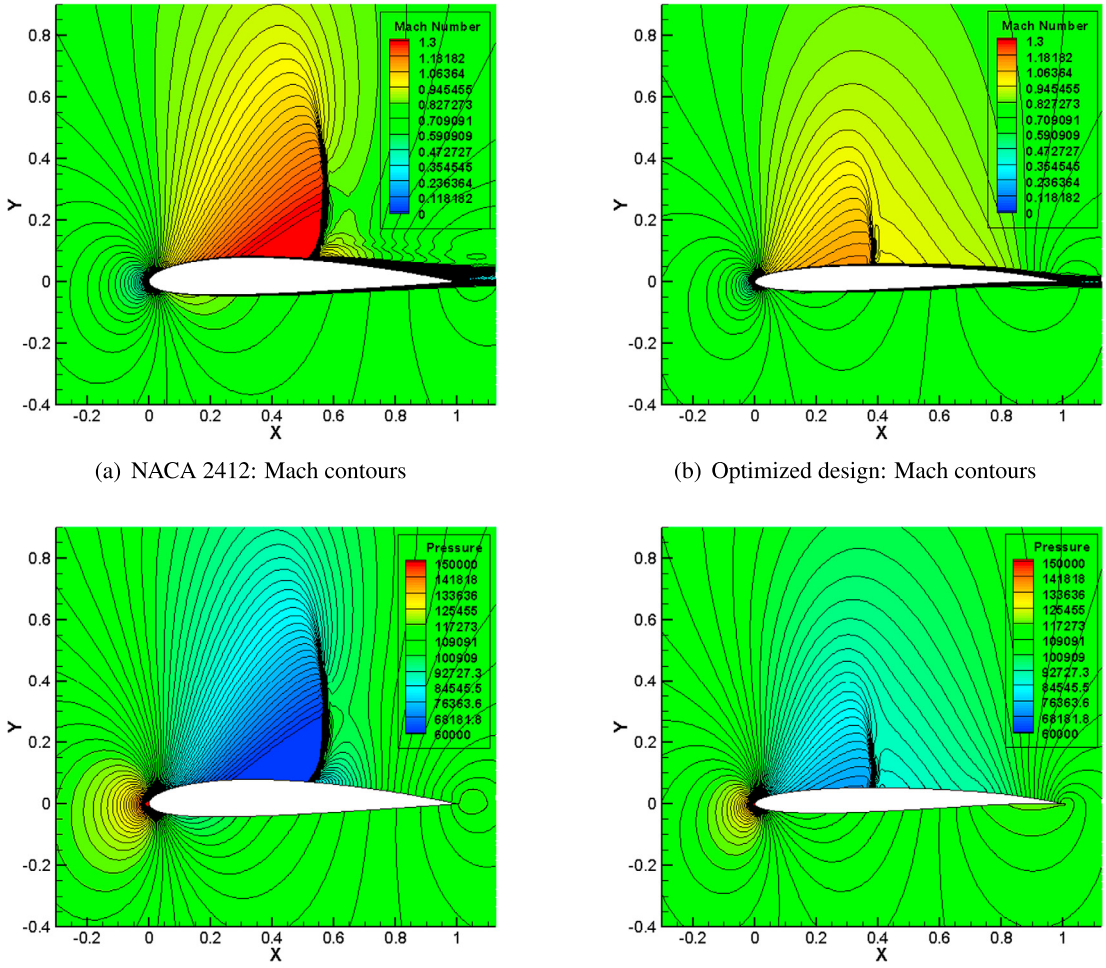

(a) NACA 2412: Mach contours

(b) Optimized design: Mach contours

(c) NACA 2412: Pressure contours

(d) Optimized design: Pressure contours

Fig. 13. Comparison of Mach & pressure contours for NACA 2412 and the optimized airfoil design at a lift coefficient of 0.55.

6. Conclusions

The objective of this paper was to present a robust optimization algorithm for computationally efficient airfoil design under mixed (inherent and epistemic) uncertainty using a multi-fidelity approach. Stochastic expansions derived from the NIPC technique are used to create surrogate models utilized in the optimization process. In this work, a combined NIPC expansion approach is used, where both the design and the mixed uncertain parameters are the independent variables of the surrogate model. In order to reduce the computational cost, the high-fidelity CFD model is replaced by a suitably corrected low-fidelity one, the latter being evaluated using the same CFD solver but with a coarser mesh. The model correction is implemented to the low-fidelity CFD solutions utilized for the construction of stochastic surrogate by using a multi-point Output Space Mapping (OSM) technique.

The proposed methodology is demonstrated for the aerodynamic optimization of NACA 4-digit airfoils at transonic flow. The objective was to reduce the mean, standard deviation and the difference in standard deviation of the drag coefficient simultaneously to obtain an airfoil shape with minimum drag that is least sensitive to the change in uncertain parameters. The Mach number is treated as a normally distributed aleatory uncertain variable with a mean of $\mu = 0.75$ and standard deviation $\sigma = 0.015$. A geometric parameter β (from the thickness distribution formula) is treated as the epistemic uncertain parameter with a specified range of $[0.17, 0.23]$. The optimization is performed such that the mean lift coefficient is greater than or equal to 0.55. Two low-fidelity models (grid levels 2 and 3 from the grid convergence study) are chosen for the robust optimization study. After the correction is applied to both the low-fidelity models, the optimization results are compared to those obtained with the surrogates created with the high-fidelity model directly.

The results of both optimization cases confirmed the effectiveness of the multi-fidelity robust optimization approach with stochastic expansions. Although the optimized design obtained by using the low-fidelity model (without correction) was comparable to that of the high-fidelity one, the statistics for the drag coefficient (for, e.g., average mean C_d, average mean σ_{C_d}, etc.) did not converge to the correct optimum. The accuracy in terms of convergence of statistics was achieved through the use of corrected low-fidelity model. As expected, corrected low-fidelity model based on grid level 3 performed better than the one based on grid level 2. In terms of computational cost, the proposed multi-fidelity technique outperforms the conventional approach that exclusively uses the high-fidelity model to create the surrogates. The design cost reduces to only 34 equivalent high-fidelity model evaluations (for CLF grid level 3) versus 168 for the conventional method. Overall this study demonstrates that the computational cost of robust design is reduced significantly by replacing the expensive high-fidelity model with a corrected low-fidelity model, without compromising on the accuracy.

Conflict of interest statement

The authors have NO affiliations with or involvement in any organization or entity with any financial interest (such as honoraria; educational grants; participation in speakers' bureaus; membership, employment, consultancies, stock ownership, or other equity interest; and expert testimony or patent-licensing arrangements), or non-financial interest (such as personal or professional relationships, affiliations, knowledge or beliefs) in the subject matter or materials discussed in this manuscript.

Acknowledgements

Funding for this research for the first two authors was provided by the NASA Grant NNX14AN17A.

References

[1] W.L. Oberkampf, J.C. Helton, C.A. Joslyn, S.F. Wojtkiewicz, S. Ferson, Challenge problems: uncertainty in system response given uncertain parameters, Reliab. Eng. Syst. Saf. 85 (1–3) (2004) 11–19.
[2] L.P. Swiler, T. Paez, R. Mayes, Epistemic uncertainty quantification tutorial, SAND 2008-6578C, Paper 294, in: Proceedings of the IMAC XXVII Conference and Exposition on Structural Dynamics, Society for Structural Mechanics, Orlando, FL, Feb. 2009.
[3] J.C. Helton, J.D. Johnson, W.L. Oberkampf, An exploration of alternative approaches to the representation of uncertainty in model predictions, Reliab. Eng. Syst. Saf. 85 (1–3) (2004) 39–71.
[4] Y. Zhang, S. Hosder, L. Leifsson, S. Koziel, Robust airfoil optimization under inherent and model-form uncertainties using stochastic expansions, AIAA-Paper 2012-0056, in: 50th AIAA Aerospace Sciences Meeting Including the New Horizon Forum and Aerospace Exposition, Nashville, TN, January 9–12, 2012.
[5] L. Leifsson, S. Koziel, Y. Zhang, S. Hosder, Low-cost robust airfoil optimization by variable-fidelity models and stochastic expansions, AIAA-Paper 2013-0631, in: 51th AIAA Aerospace Sciences Meeting Including the New Horizon Forum and Aerospace Exposition, Grapevine, TX, January 7–10, 2013.
[6] J. Bandler, Q. Cheng, S. Dakroury, A. Mohamed, M. Bakr, K. Madsen, J. Sondergaard, Space mapping: the state of the art, IEEE Trans. Microw. Theory Tech. 52 (1) (2004) 337–361.
[7] S. Koziel, J. Bandler, K. Madsen, A space mapping framework for engineering optimization: theory and implementation, IEEE Trans. Microw. Theory Tech. 54 (10) (2006) 3721–3730.
[8] S. Koziel, Q. Cheng, J. Bandler, Space mapping, IEEE Microw. Mag. 9 (6) (2008) 105–122.
[9] Q. Cheng, S. Koziel, J. Bandler, Simplified space mapping approach to enhancement of microwave device models, Int. J. RF Microw. Comput.-Aided Eng. 16 (5) (2006) 518–535.
[10] S. Hosder, R.W. Walters, M. Balch, Point-collocation nonintrusive polynomial chaos method for stochastic computational fluid dynamics, AIAA J. 48 (12) (2010) 2721–2730.
[11] B. Bettis, S. Hosder, Quantification of uncertainty in aerodynamic heating of a reentry vehicle due to uncertain wall and freestream conditions, AIAA-Paper 2010-4642, in: 10th AIAA Joint Thermophysics and Heat Transfer Conference, Chicago, IL, June 2010.
[12] N. Wiener, The homogeneous chaos, Am. J. Math. 60 (4) (1994) 897–936.
[13] D. Xiu, G.E. Karniadakis, Modeling uncertainty in flow simulations via generalized polynomial chaos, J. Comput. Phys. 187 (1) (2003) 137–167.
[14] J. Witteveen, H. Bijl, Modeling arbitrary uncertainties using Gram–Schmidt polynomial chaos, AIAA-Paper 2006-896, in: 44th AIAA Aerospace Sciences Meeting and Exhibit, Reno, NV, January 9–12, 2006.
[15] M.S. Eldred, C.G. Webster, P.G. Constantine, Evaluation of non-intrusive approaches for Wiener–Askey generalized polynomial chaos, AIAA-Paper 2008-1892, in: 10th AIAA Non-Deterministic Approaches Forum, Schaumburg, IL, April 2008.
[16] R.W. Walters, L. Huyse, Uncertainty Analysis for Fluid Mechanics with Applications, Tech. rep., ICASE 2002-1, NASA/CR-2002-211449, NASA Langley Research Center, Hampton, VA, 2002.
[17] H.N. Najm, Uncertainty quantification and polynomial chaos techniques in computational fluid dynamics, Annu. Rev. Fluid Mech. 41 (2009) 35–52.
[18] S. Hosder, R.W. Walters, Non-intrusive polynomial chaos methods for uncertainty quantification in fluid dynamics, AIAA-Paper 2010-0129, in: 48th AIAA Aerospace Sciences Meeting, Orlando, FL, January 4–7, 2010.
[19] S. Hosder, R.W. Walters, M. Balch, Efficient sampling for non-intrusive polynomial chaos applications with multiple input uncertain variables, AIAA-Paper 2007-1939, in: 9th AIAA Non-Deterministic Approaches Conference, Honolulu, HI, April, 2007.
[20] ANSYS FLUENT Tutorial Guide, ver 14.5, ANSYS Inc, Southpointe, 275, Technology Drive, Canonsburg, PA 15317, 2011.
[21] J.D. Anderson, Fundamentals of Aerodynamics, 4th edition, McGraw–Hill, New York, 2010.
[22] P.R. Spalart, S.R. Allmaras, A one equation turbulence model for aerodynamic flows, AIAA-Paper 92-0439, in: 38th AIAA Aerospace Sciences Meeting and Exhibit, Reno, NV, January 6–9, 1992.
[23] T.J. Barth, T.H. Pulliam, P.G. Buning, Navier–Stokes computations for exotic airfoils, AIAA-Paper 1985-0109, in: 23rd AIAA Aerospace Sciences Meeting, Reno, NV, 1985, http://arc.aiaa.org/doi/abs/10.2514/6.1985-109.
[24] S. Hosder, B. Grossman, R.T. Haftka, W.H. Mason, L.T. Watson, Quantitative relative comparison of CFD simulation uncertainties for a transonic diffuser problem, Comput. Fluids 35 (2006) 1444–1458, http://www.sciencedirect.com/science/article/pii/S0045793005000757.
[25] I.H. Abbott, A.E. Von Doenhoff, Theory of Wing Sections, Dover Publications, 1959.